

RESEARCH

Open Access



Reproducibility and repeatability of a semi-automated pipeline to quantify trapeziometacarpal joint angles using dynamic computed tomography

Michael T. Kuczynski^{1,2}, Kendra Wang^{2,3,4}, Justin J. Tse^{2,3}, Tomasz Bugajski^{1,2} and Sarah L. Manske^{1,2,3*}

Abstract

Background: The trapeziometacarpal (TMC) joint is a mechanically complex joint and is commonly affected by musculoskeletal diseases such as osteoarthritis. Quantifying in vivo TMC joint biomechanics, such as joint angles, with traditional reflective marker-based methods can be difficult due to the joint's location in the hand. Dynamic computed tomography (CT) can facilitate the quantification of TMC joint motion by continuously capturing three-dimensional volumes over time. However, post-processing of dynamic CT datasets can be time intensive and automated methods are needed to reduce processing times to allow for application to larger clinical studies. The purpose of this work is to introduce a fast, semi-automated pipeline to quantify joint angles from dynamic CT scans of the TMC joint and evaluate the associated error in joint angle and translation computation by means of a reproducibility and repeatability study.

Methods: Ten cadaveric hands were scanned with dynamic CT using a passive motion device to move thumbs in a radial abduction–adduction motion. Static CT scans and high-resolution peripheral quantitative CT scans were also acquired to generate high-resolution bone meshes. Abduction–adduction, flexion–extension, and axial rotation angles were computed using a joint coordinate system. Reproducibility and repeatability were assessed using intraclass correlation coefficients, Bland–Altman analysis, and root mean square errors. Target registration errors were computed to evaluate errors associated with image registration.

Results: We found good repeatability for flexion–extension, abduction–adduction, and axial rotation angles. Reproducibility was moderate for all three angles. Joint translations exhibited greater repeatability than reproducibility. Specimens with greater joint degeneration had lower repeatability and reproducibility. We found that the difference in resulting joint angles and translations were likely due to differences in segment coordinate system definition between multiple raters, rather than due to registration errors.

Conclusions: The proposed semi-automatic processing pipeline was fast, repeatable, and moderately reproducible when quantifying TMC joint angles and translations. This work provides a range of errors for TMC joint angles from dynamic CT scans using manually selected anatomical landmarks.

*Correspondence: smanske@ucalgary.ca

² McCaig Institute for Bone and Joint Health, University of Calgary, 3280 Hospital Drive, N.W., Calgary, AB T2N 4Z6, Canada
Full list of author information is available at the end of the article



© The Author(s) 2022. **Open Access** This article is licensed under a Creative Commons Attribution 4.0 International License, which permits use, sharing, adaptation, distribution and reproduction in any medium or format, as long as you give appropriate credit to the original author(s) and the source, provide a link to the Creative Commons licence, and indicate if changes were made. The images or other third party material in this article are included in the article's Creative Commons licence, unless indicated otherwise in a credit line to the material. If material is not included in the article's Creative Commons licence and your intended use is not permitted by statutory regulation or exceeds the permitted use, you will need to obtain permission directly from the copyright holder. To view a copy of this licence, visit <http://creativecommons.org/licenses/by/4.0/>. The Creative Commons Public Domain Dedication waiver (<http://creativecommons.org/publicdomain/zero/1.0/>) applies to the data made available in this article, unless otherwise stated in a credit line to the data.

Keywords: Joint angle, Cadaver, Dynamic computed tomography, Trapeziometacarpal joint

Background

The trapeziometacarpal (TMC) joint at the base of the thumb provides the unique prehensile ability of the hand, allowing for grasping and pinching. Defined as a biconcave-convex or saddle shaped joint [1] the TMC joint is supported by 16 ligaments [2] and has been shown to experience contact forces of up to 120 kg during strong grasps [3]. The biomechanical complexity of the TMC joint increases the joint's predisposition to the development of joint diseases such as osteoarthritis (OA), wherein ligament laxity [4] and repetitive motions [5–7] have been shown to increase the risk of development of OA. As such, better understanding the biomechanical behaviour of the TMC joint may provide new information in the study of diseases of the hand. However, the quantification of joint biomechanics in the TMC joint is often difficult *in vivo* due to the small size of bones and inaccessibility for skin-based marker placement (*e.g.*, carpal bones). To quantify joint motion in three dimensions (3D) in motion capture systems, reflective skin-based markers are placed on each bone segment in three spatial planes. However, non-invasively placing reflective markers on the TMC joint is often not possible, particularly for the trapezium located in the wrist. The use of non-invasive medical imaging technologies, such as computed tomography (CT), can provide 3D representations of joints. While previous imaging studies have shown changes in joint space and contact area [8, 9] in OA of the TMC joint, these studies have been limited to static imaging, which may not represent true joint biomechanics, particularly in diseased joints. Capturing true dynamic TMC joint motion may improve our understanding of TMC joint biomechanics and how altered joint biomechanics may relate to the development of diseases such as OA. Dynamic CT is a technique that has been commonly used in cardiac and respiratory imaging and is now emerging as a potential technique for imaging joint biomechanics *in vivo*. Dynamic CT provides 3D images over time, allowing for more accurate estimates of hand joint kinematics than is possible with motion capture systems. Several recent studies have utilized dynamic CT for various musculoskeletal applications and have demonstrated the feasibility of dynamic CT imaging for measuring joint motion (*i.e.*, rotations and translations), displacements, and even estimates of joint contact [10–14]. However, post-processing methods for dynamic CT datasets published to date are time intensive, reducing the practicality of applying this technique to larger clinical studies. In one study, 120 h were required to process a single TMC joint

for a single movement [11], highlighting the need for fast, automated tools to process data from dynamic CT. Dynamic CT protocols typically suffer from low spatial resolution when compared to static CT scans, requiring additional post-processing to overcome these limitations. These additional post-processing steps often introduce new sources of error from image processing techniques, such as image registration between dynamic CT frames or registration between static, high-resolution CT images to dynamic CT frames.

When describing joint motion, segment coordinate systems (SCS) must first be defined. Using 3D bone meshes obtained from CT imaging, SCSs can be defined using points placed on anatomical landmarks (AL) to define each axis of the SCS, similar to the process used in motion capture systems. Previous motion capture studies using skin-based reflective markers have shown that the subjective task of manually placing markers on ALs can cause large variations in the resulting joint angle measurements [15]. These errors are often due to skin motion artifacts and inconsistencies between raters. While placing ALs directly on the bony anatomy in dynamic CT datasets removes the effect of skin motion artifacts, inconsistencies between raters may still produce errors in resulting joint biomechanics. Thus, the error associated with manually placed ALs in dynamic CT datasets warrants further investigation.

The purpose of this study was to introduce a fast, semi-automated pipeline to measure TMC joint angles from dynamic CT scans, and to evaluate the repeatability and reproducibility of manual AL placement on resulting joint angles. As a secondary analysis, we evaluated the effect of manual AL placement on the repeatability and reproducibility of joint translations. For this study, we define the repeatability as the precision of resulting joint angles and translations after repeated AL placement by a single rater. Reproducibility was defined as the precision of resulting joint angles and translations after AL placement by three separate raters. It was hypothesized that manually placed ALs will provide excellent repeatability and moderate reproducibility in resulting joint angles and translations.

Materials and methods

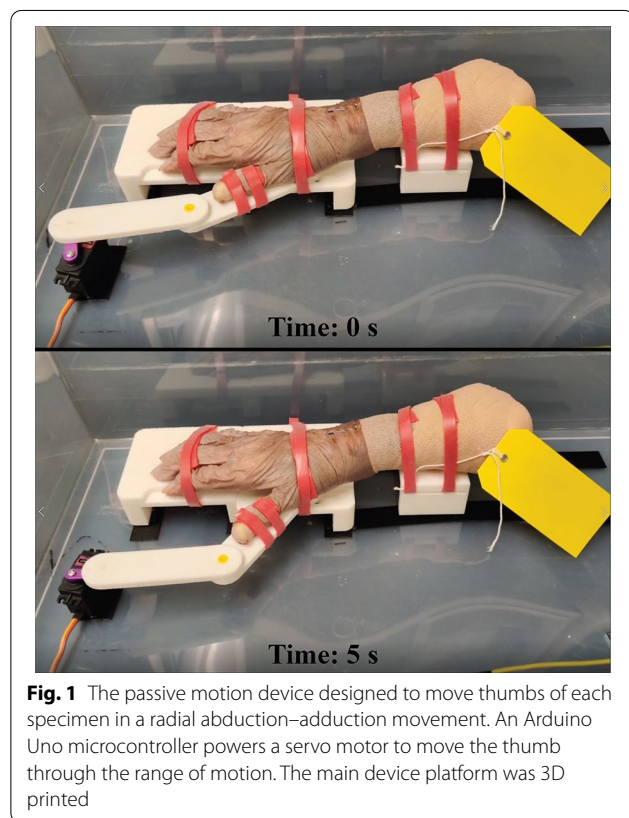
Specimen preparation

Ten cadaveric hands were acquired from the Advanced Technical Skills Simulation Laboratory at the University of Calgary (right hands, 4 female, 6 male, mean age: 81.6 ± 13.9 years). Each specimen contained the entire

hand, wrist, and a portion of the forearm (Fig. 1). The medical history of each specimen was not obtained for this study. All methods were performed in accordance with guidelines set by the Conjoint Health Research Ethics Board at the University of Calgary (REB20-0039).

Experimental setup

Prior to scanning, each specimen was securely strapped onto a custom 3D-printed passive motion device designed to move the thumb in a radial abduction–adduction motion (*i.e.*, functional flexion–extension) (Fig. 1). An Arduino Uno microcontroller powered a servo motor using software developed using C++ (Arduino IDE, v1.8.13). A resting position was defined as laying all fingers flat, pointing forward, and pressed together to minimize space between fingers. From several pilot scans, a time of 5 s for the thumb to move from a resting position to a fully abducted position and back to resting position, was determined to qualitatively minimize motion artifact. Range of motion was not standardized between specimens as we were only interested in errors associated between and within raters, not errors due to the passive motion device.



Imaging protocol

Each specimen underwent dynamic CT scanning (GE Revolution HD GSI scanner, GE Healthcare, Chicago, USA) at the Centre for Mobility and Joint Health, University of Calgary. Dynamic CT scans were performed using 120 kVp, 100 mA, 0.4 s/gantry revolution, 40 mm longitudinal coverage, and $0.625 \times 0.625 \times 2.5$ mm voxel size. Each specimen was scanned for 15 s, resulting in approximately three radial abduction–adduction movements and 60 frames of data. Dynamic CT images were resampled to 0.625 mm^3 isotropic voxels. Due to scanner spatial resolution and longitudinal coverage limitations, static CT scans (120 kVp, 150 mA, $0.375 \times 0.375 \times 0.625$ mm voxel size, and 0.531 pitch factor) were also performed to ensure the TMC joint was fully captured. Additionally, high-resolution peripheral quantitative CT images (HR-pQCT, XtremeCT II, Scanco Medical, Brüttisellen, Switzerland) were acquired to provide greater detail in the bony anatomy when selecting ALs. HR-pQCT scans were obtained using a standard *in vivo* imaging protocol (68 kVp, 1470 μA , 43 ms integration time, 900 projections/180°, 61 μm^3 voxels) with an extended longitudinal coverage to capture the full TMC joint.

Image processing

All processing was performed using custom Python scripts (v.3.8.5) using the VTK (v8.2.0, Schroeder et al. [16]), ITK (v5.2.1, McCormick et al. [17]), and SimpleITK (v2.0.2, Lowekamp et al. [18]) libraries. All scripts used in this study are made available through a public GitHub repository (<https://github.com/ManskeLab/DYNACT>). Binary masks for the first metacarpal (MC1) and trapezium (TRP) were obtained from HR-pQCT images (Fig. 2). Then, a series of image registration steps were performed to move the bone masks to the dynamic CT space (Fig. 3). Each bone was processed individually and recombined in the dynamic CT image space.

Image segmentation

Grayscale HR-pQCT images were first binarized using a fixed global threshold ($520 \leq \text{threshold} \leq 6600$ Hounsfield units). Next, binary smoothing and a series of binary morphological operations (binary opening and closing) removed the binary components resulting from noise. A manual step was occasionally required to disconnect the MC1 and TRP bones when joint space was very narrow. Connected component labelling was then applied to isolate each bone. Further morphological operations and mesh smoothing were performed to obtain the final bone mask (Fig. 2). These bone masks were then used to select ALs.

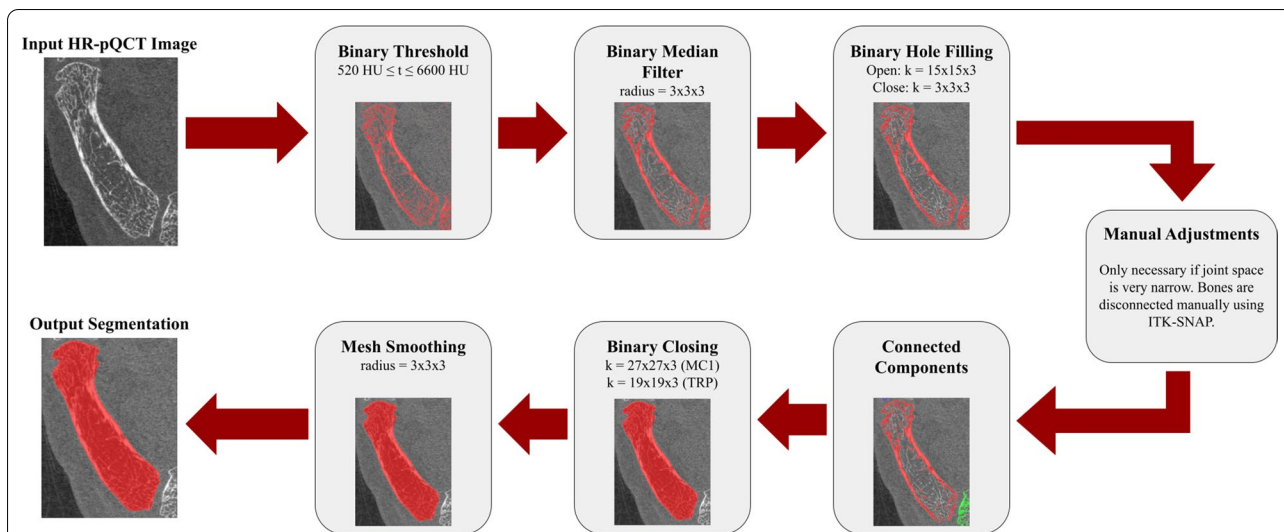


Fig. 2 Processing pipeline for binarizing the TMC joint from HR-pQCT scans. The pipeline outlined is run for the first metacarpal and trapezium separately. The segmentation pipeline is semi-automated, only requiring manual intervention if the automated segmentation cannot differentiate between the first metacarpal and trapezium bones due to narrow joint space. The binary threshold (t) is provided in Hounsfield Units (HU) and the kernel size (k) for binary morphological operations are provided for the first metacarpal (MC1) and trapezium (TRP)

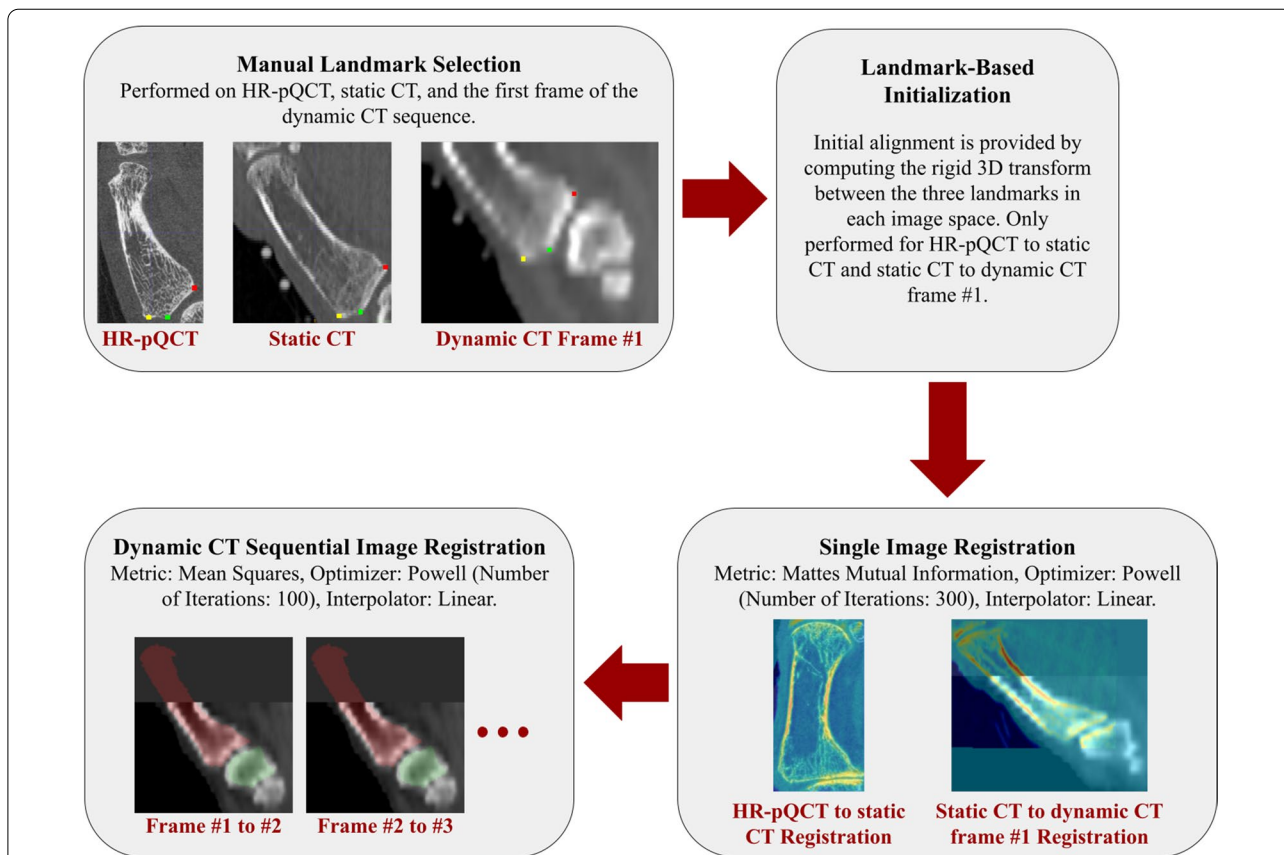


Fig. 3 Overview of the image registration pipeline. Intensity-based registration is used to generate rigid, 3D transformation matrices that transform binary masks from the high-resolution CT scans to each frame of the dynamic CT dataset. Anatomical landmarks chosen in the high-resolution image space by each rater are also transformed to each dynamic CT frame using the same rigid transformation

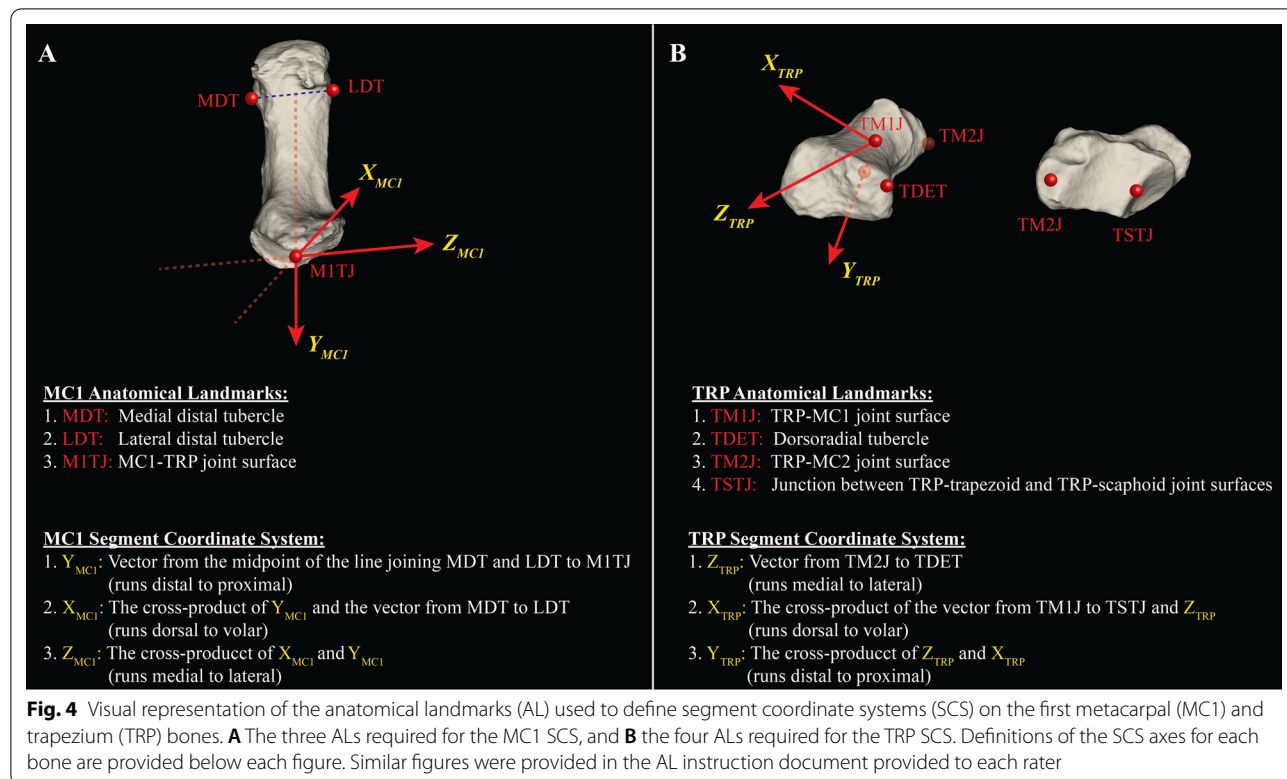
Image registration

Bone masks and ALs were rigidly transformed to each frame of the dynamic CT scan in a three-step process (Fig. 3). This was required as the drastic resolution change from HR-pQCT to dynamic CT did not visually produce adequate alignment when registered directly. First, three manually placed landmarks were selected on each grayscale image (HR-pQCT, static CT, and the first frame of the dynamic CT scan) to generate an initial transformation between image spaces. Final image alignment was obtained automatically using intensity-based image registration between each set of images. Registration for HR-pQCT to static CT and static CT to the first dynamic CT frame used a Mattes Mutual Information metric [19], Powell optimizer, linear interpolator, and rigid 3D transform. Image registration between dynamic CT frames was performed using a sequential registration approach that utilized the position of the previous frame to provide initial alignment. A mean squares metric, Powell optimizer, linear interpolator, and rigid 3D transform were used to obtain binary masks and SCSs in each dynamic CT frame. Each registration provided a transformation matrix that could be used to transform the bone masks and ALs to the dynamic CT image space.

Joint kinematics

Segment coordinate system definition

Joint angles in the dynamic CT image space were computed using a joint coordinate system (JCS) representation [20] previously defined for the TMC joint that minimizes kinematic cross-talk [21] (Fig. 4). To establish a SCS, a custom visualization tool was developed using Python and VTK to visualize each bone model in 3D, allowing for AL selection. Three ALs were defined on the MC1: (1) LDT: centre of the lateral distal MC1 tubercle, (2) MDT: centre of the medial distal MC1 tubercle, and (3) MITJ: centre of the MC1-TRP joint surface. The origin of the MC1 SCS was defined as MITJ. Four ALs were defined on the TRP: (1) TM1J: centre of TRP-MC1 joint surface, (2) TM2J: centre of the TRP-second metacarpal joint surface, (3) TSTJ: centre of the junction between the TRP-trapezoid and TRP-scaphoid joint surfaces, and (4) TDET: distal end of the dorsoradial tubercle (viewed laterally). The origin of the TRP SCS was defined as TM1J. The definition of the SCSs for each bone have been previously described [21] and are shown in Fig. 4. ALs were later transformed to the dynamic CT image space where JCSs were defined in each frame.



Joint coordinate system definition

In accordance with a previous JCS definition in the TMC joint [21], the following mobile axis sequence was used: flexion–extension about the Z-axis of the TRP SCS (Fig. 4, Z_{TRP}), abduction–adduction about the X-axis of the MC1 SCS (Fig. 4, X_{MC1}), and axial rotation about a floating axis mutually orthogonal to Z_{TRP} and X_{MC1} . ALs were transformed to each dynamic CT frame using transformation matrices obtained from the image registration process defined above (Fig. 3). Orientation of the MC1 relative to the TRP (R_{TRP_MC1}) was then computed by decomposing the ZYX mobile axis sequence:

$$R_{TRP_MC1} = R_{X_{MC1}} \cdot R_Y \cdot R_{Z_{TRP}}$$

$$= \begin{bmatrix} \cos(\gamma)\cos(\beta) & \sin(\gamma)\cos(\alpha) + \cos(\gamma)\sin(\beta)\sin(\alpha) & \sin(\gamma)\sin(\alpha) - \cos(\alpha)\cos(\gamma)\sin(\beta) \\ -\sin(\gamma)\cos(\beta) & \cos(\gamma)\cos(\alpha) - \sin(\gamma)\sin(\beta)\sin(\alpha) & \sin(\alpha)\cos(\gamma) + \sin(\gamma)\sin(\beta)\cos(\alpha) \\ \sin(\beta) & -\sin(\alpha)\cos(\beta) & \cos(\beta)\cos(\alpha) \end{bmatrix}$$

where α is the abduction–adduction angle (abduction is positive), β is the axial rotation angle (internal rotation is positive), and γ is the flexion–extension angle (flexion is positive). Joint translation was computed by determining the translation of the MC1 SCS origin (landmark M1T) with respect to the TRP SCS [22].

Reproducibility and repeatability

Three raters (MTK, JJT, and TB) selected ALs on HR-pQCT bone masks to evaluate the reproducibility of the processing pipeline. One rater (MTK) selected ALs in three repeated trials on all images to evaluate repeatability. Each rater was provided with a document outlining the locations of each AL. The document described each AL, showing the surface on which to place the AL and examples of AL placement on one specimen. Each rater's ALs were transformed to the dynamic CT image space to compute joint angles and translations and compare results between raters.

Image registration accuracy

Experimental setup

As the post-processing pipeline used to quantify joint angles relied on intensity-based image registration, we estimated the accuracy of the image registration by computing target registration errors (TRE). Three fiducial markers (borosilicate beads, 4.76 mm diameter) were implanted into the MC1 bone of one specimen. An incision along the anatomical snuffbox was made and fiducial markers were implanted by drilling holes into the bone and gluing beads into place.

Target registration error

The 3D rigid transformation between image spaces defined by aligning the centroids of the fiducial markers was considered as the gold-standard transformation

(T_{GS}). Fiducial markers were binarized manually using ITK-SNAP (v3.8.0) [23] and centroids of each fiducial marker in each image space were computed. Then, the TRE is defined as the difference between T_{GS} and the transformation resulting from the intensity-based registration (T_{IR}), in a least squares sense. This calculation was performed over all n voxels (v_i) of the moving image (Eq. 1).

$$TRE^2 = \sum_{i=0}^n |T_{GS}(v_i) - T_{IR}(v_i)|^2 \quad (1)$$

The accuracy of the TRE is limited by the accuracy of the gold-standard transformation. To estimate the error associated with the gold-standard transformation, the fiducial registration error (FRE) was first calculated using three manually selected landmarks on the bony geometry, referred to as targets. The root mean square (RMS) difference between the centroids of these targets and the fiducial markers provides an estimate of the FRE (Eq. 2), which is used to estimate the fiducial localization error (FLE) (Eq. 3) [24]. Finally, an estimate of the TRE for the T_{GS} is calculated using the principal axes (PA) of the fiducial marker distribution (Eq. 4).

$$FRE^2 = \sqrt{\frac{1}{n_f} \sum_{i=0}^{n_f} (c_i - \hat{c}_i)^2} \quad (2)$$

$$FLE = \sqrt{\frac{n_f}{n_f - 2}} FRE \quad (3)$$

$$TRE^2(p) \approx \frac{FLE^2}{n_f} \left(1 + \frac{1}{3} \sum_{i=1}^3 \frac{d_i^2}{f_i^2} \right) \quad (4)$$

where n_f is the number of fiducial markers, c_i is the centroid of each fiducial marker, \hat{c}_i is the centroid of the target, p is the target location, d_i is the distance from the centroid of the target to the PA, and f_i is the RMS distance from each fiducial marker's centroid to the PA.

Statistical analysis

All statistical analyses were performed using R (v.4.1.1) [25] and SPSS (v.28.0.0.0) [26]. Inter- and intra-rater

reliability coefficients (ICC), Bland–Altman analysis, and frame-by-frame RMS error (RMSE) of joint angles between raters were calculated to evaluate reproducibility and repeatability. Inter-rater ICC was modelled as a two-way, random effects, absolute agreement, single measurement model. Intra-rater ICC was modelled as a two-way, mixed effects, absolute agreement, single measurement model. Agreement between and within raters was interpreted as follows: excellent agreement ($ICC \geq 0.9$), good agreement ($0.75 \geq ICC > 0.9$), moderate agreement ($0.5 \geq ICC > 0.75$), and poor agreement ($ICC < 0.5$) [27]. Bland–Altman analysis was performed by comparing each rater’s angle results to the mean angles between all raters. A linear regression of each rater’s Bland–Altman results was used to evaluate the slope of each rater’s angles compared to the mean. As a secondary analysis, frame-by-frame RMSE of joint translations were calculated for each spatial plane.

To evaluate the error in SCS definition between raters, the orientation difference between SCS axes was calculated between each pair of raters. First, the dot product between corresponding SCS axes was computed (e.g., $X_{SCS_1} \cdot X_{SCS_2}$, $X_{SCS_1} \cdot X_{SCS_3}$, etc.) in the HR-pQCT image space and again in each of the 60 dynamic CT frames. Then, for each SCS axis and for each pair of raters, the RMSE between the HR-pQCT SCS orientation difference and each dynamic CT SCS

orientation difference was computed, resulting in 60 RMSE values. This process was then repeated for each specimen.

Results

Joint kinematics

To compare the TMC joint range of motion with previous studies, the mean joint angle across all specimens and across all raters is provided along with the angle range. Mean joint angles were $40.7^\circ \pm 5.8^\circ$ (range: 20.0° to 53.2°) for abduction–adduction, $-16.3^\circ \pm 7.1^\circ$ (range: -28.4° to -5.2°) for flexion–extension, and $-5.4^\circ \pm 4.1^\circ$ (range: -13.2° to 4.6°) for axial rotation.

Joint kinematics reproducibility and repeatability

Intra-rater ICC values had the following ranges across all specimens: abduction–adduction: 0.64–0.91, flexion–extension: 0.50–0.99, axial rotation: 0.46–0.98. Inter-rater ICC values had the following ranges: abduction–adduction: 0.21–0.90, flexion–extension: 0.07–0.71, axial rotation: 0.12–0.85. All ICC values are presented in Fig. 5. A comparison of joint angles from one specimen are shown in Fig. 6. Results of the Bland–Altman analysis for one specimen are shown in Fig. 7. While roughly half of the slopes were statistically significantly different than zero, all regression lines had slopes with small values (< 0.06 , absolute value).

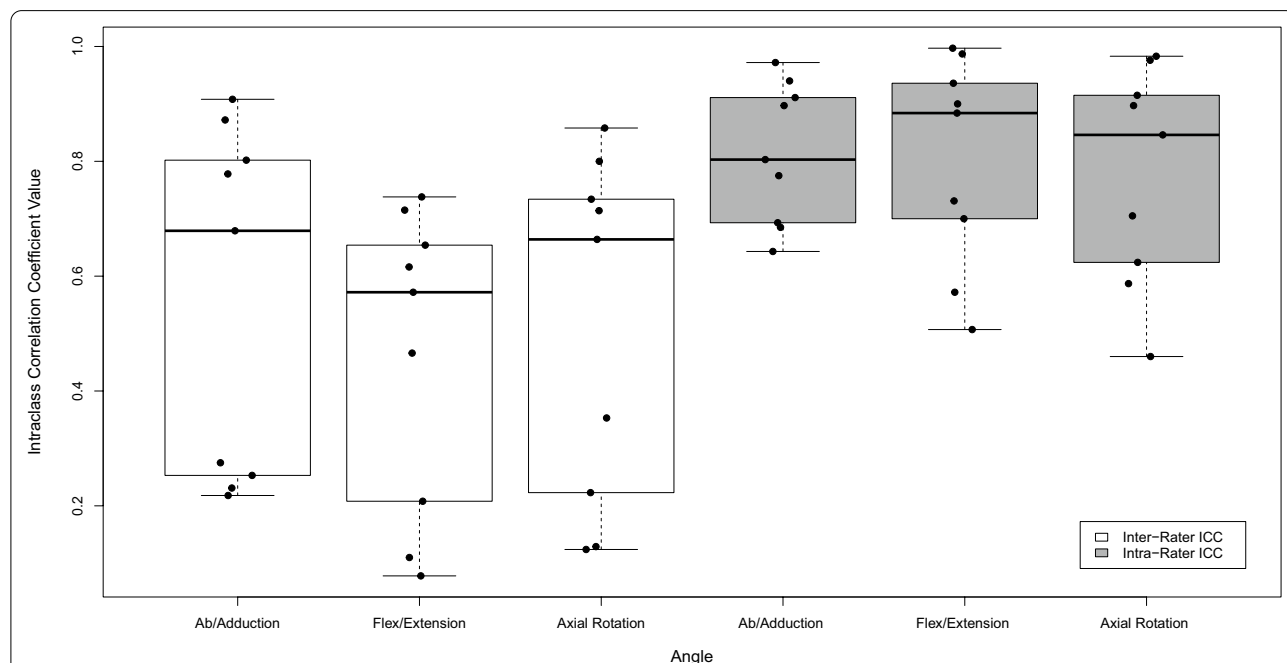
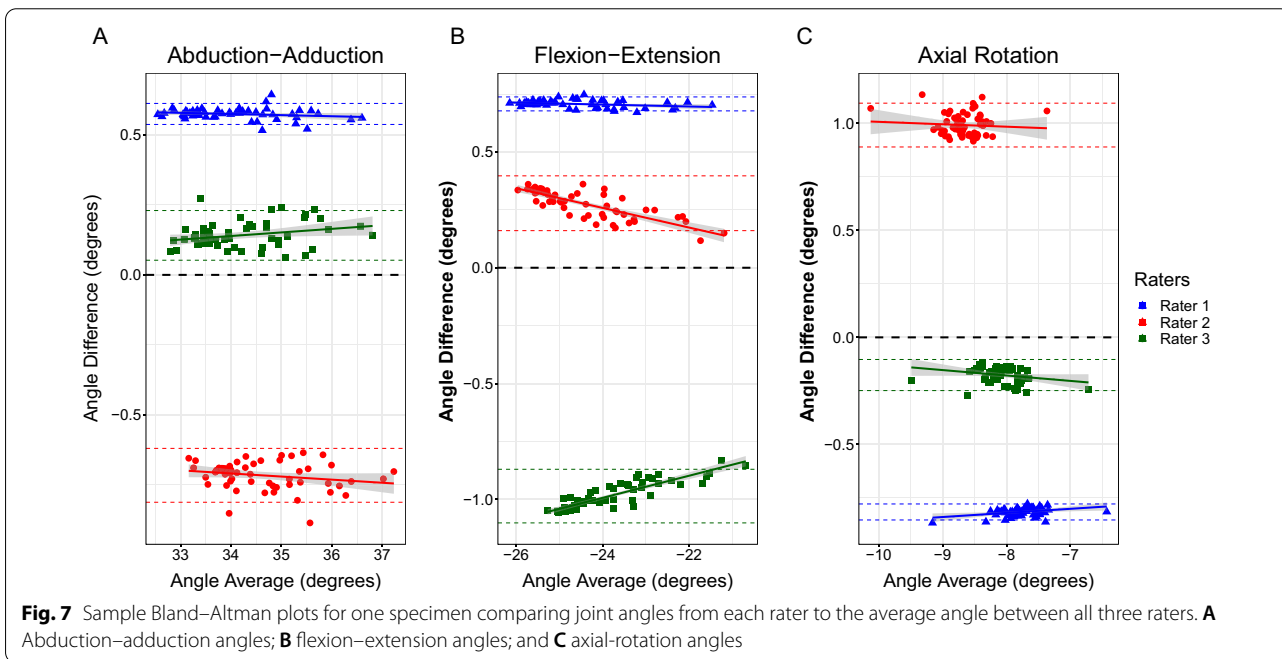
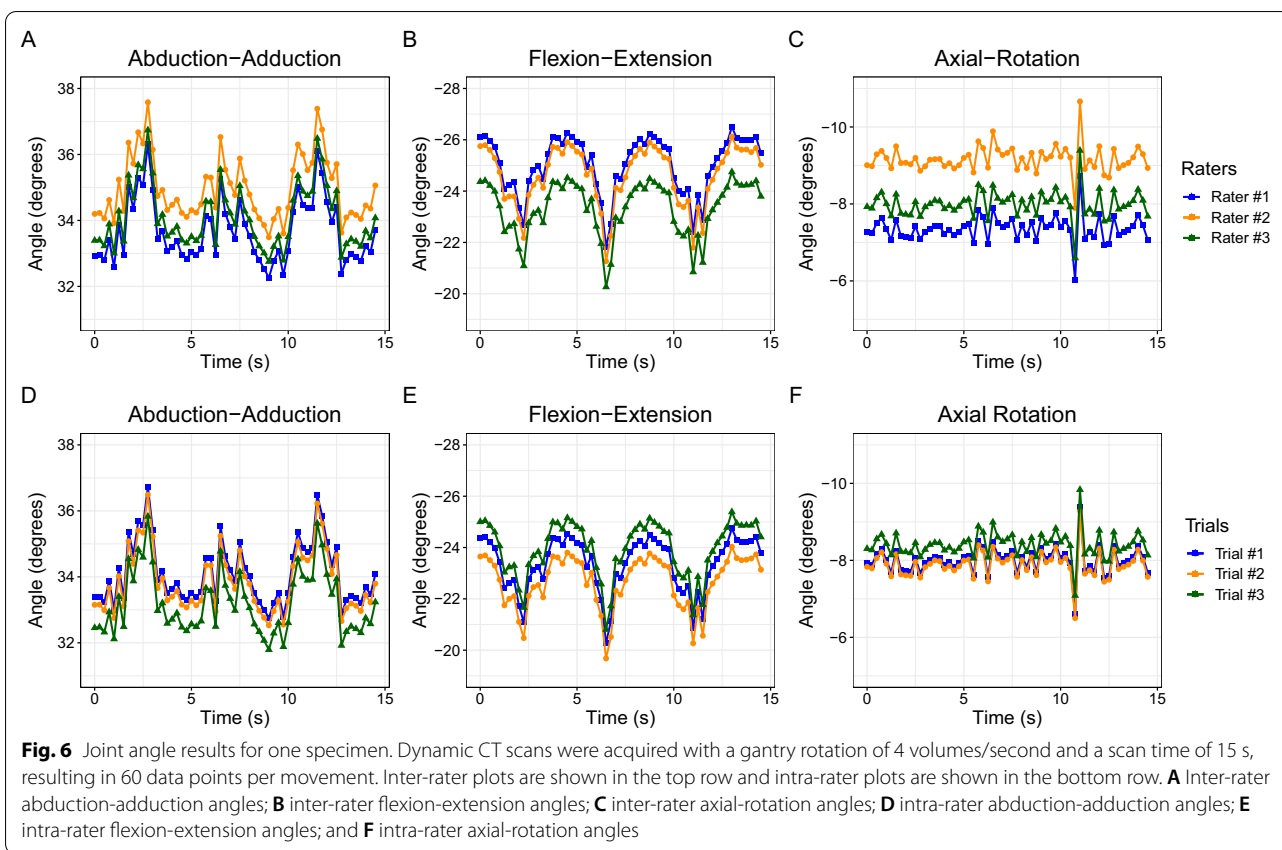
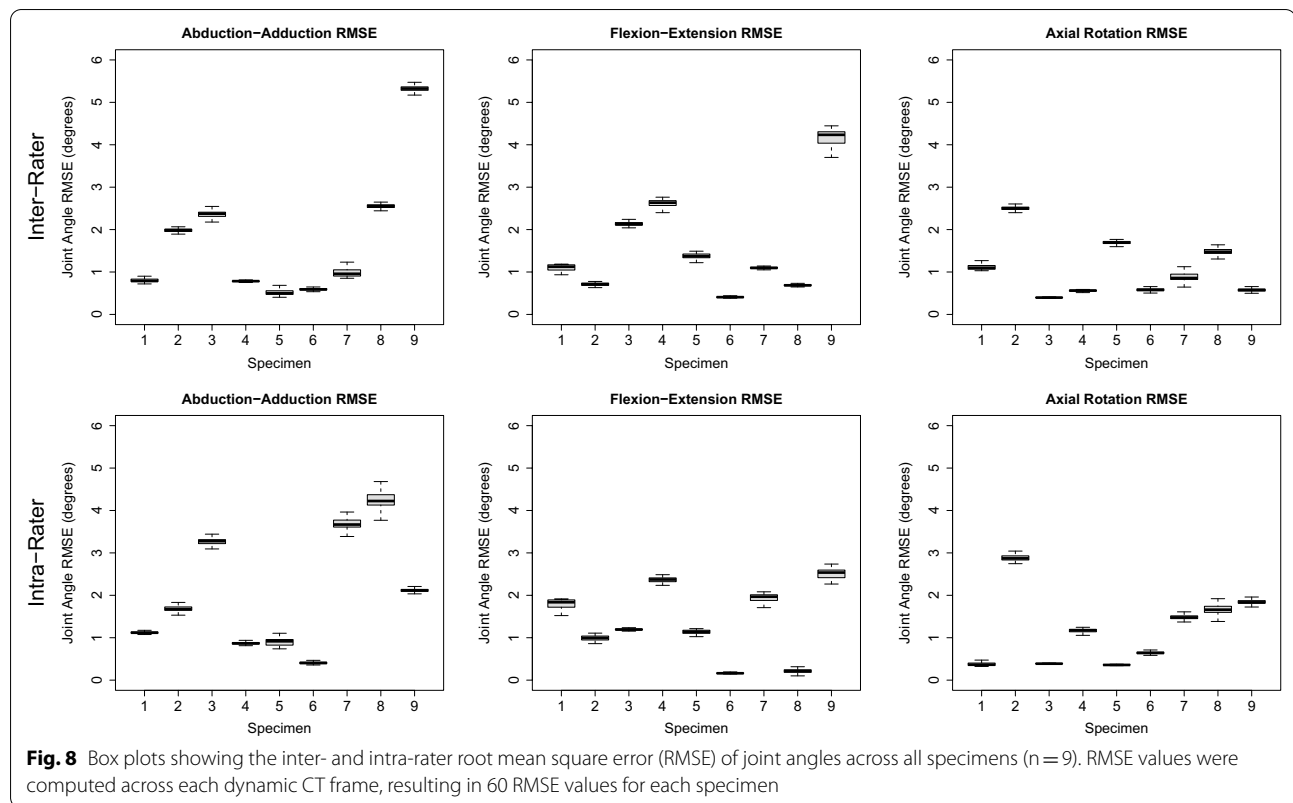


Fig. 5 Box plot of inter- and intra-rater intraclass correlation coefficients (ICC) for each measured angle, across all specimens (n=9). Inter-rater ICCs were calculated using a two-way, random effects, absolute agreement model. Intra-rater ICCs were calculated using a two-way, mixed effects, absolute agreement model. Intra-rater ICC values showed better agreement than inter-rater ICC values



Average RMSEs are presented in Fig. 8 and intra-rater RMSE tended to be lower than inter-rater RMSE. Average inter-rater RMSE across specimen was $1.76^{\circ} \pm 1.54^{\circ}$

for abduction-adduction, $1.58^{\circ} \pm 1.19^{\circ}$ for flexion-extension, and $1.08^{\circ} \pm 0.69^{\circ}$ for axial rotation. Average intra-rater RMSE across specimen was $2.03^{\circ} \pm 1.38^{\circ}$ for



abduction–adduction, $1.36^{\circ} \pm 0.84^{\circ}$ for flexion–extension, and $1.19^{\circ} \pm 0.85^{\circ}$ for axial rotation. The following joint translation RMSEs were computed: $X < 1.44$ mm, $Y < 1.55$ mm, $Z < 2.15$ mm for inter-rater RMSE, and $X < 1.26$ mm, $Y < 0.83$ mm, $Z < 1.05$ mm for intra-rater RMSE.

Image co-registration accuracy

TREs for the manually selected targets were found to be 0.0010, 0.0010, and 0.0011 mm for the registration between HR-pQCT and static CT, 0.64, 0.43, and 0.66 mm for the registration between static CT and the first dynamic CT frame, and 0.33, 0.33, and 0.27 mm for the registration between the first and second dynamic CT frame. The error associated with the gold-standard transformation (*i.e.*, using the centroids of the implanted fiducial markers) was found to be 0.00049 mm for the image registration between HR-pQCT and static CT, 0.31 mm for image registration between static CT and the first frame of the dynamic CT dataset, and 0.62 mm between the first and second dynamic CT frames.

When analyzing the orientation difference between each bone’s SCS axes in the HR-pQCT and dynamic CT image space, we found that the RMSE between image

spaces for each dynamic CT frame, for all pairs of raters, was less than $1.3e^{-11}$ mm (data not shown).

Discussion

We propose a semi-automated pipeline to quantify joint motion in the TMC joint using dynamic CT. Our joint angle results (Table 1) fall within range of previously reported TMC joint angles for similar thumb movements [1, 21, 28]. While much of this pipeline has been automated, SCSs were defined using manually placed ALs. Contrary to our original hypothesis, we found good repeatability (*i.e.*, intra-rater) and moderate reproducibility (*i.e.*, inter-rater) for joint angle computation. Additionally, we found joint translational errors to be lower when ALs were selected by a single rater as compared to ALs selected by multiple raters, for each plane of motion. However, we found that within rater results exhibited lower variability (Fig. 5, Intra-Rater ICC) compared to between rater results (Fig. 5, Inter-Rater ICC) for all joint angles. Inter-rater flexion–extension angles demonstrated lower ICC values when compared to inter-rater abduction–adduction angles. Trapezium morphology has been shown to change with age and disease state [29], which may lead to greater variability between AL placement and explain the decreased inter-rater ICC for

Table 1 Mean joint angles across three raters

Specimen	Joint angle mean [Range] (degrees)		
	Abduction–adduction	Flexion–extension	Axial rotation
1	34.2 [32.8, 36.9]	−24.3 [−25.8, −21.1]	−8.2 [−9.6, −6.8]
2	43.4 [41.1, 45.7]	−17.5 [−19.8, −16.0]	−4.4 [−6.5, −2.6]
3	46.9 [44.3, 48.6]	−11.9 [−12.8, −10.3]	−10.6 [−12.9, −9.7]
4	46.3 [43.7, 49.8]	−3.1 [−5.2, −1.0]	−10.4 [−13.2, −7.9]
5	33.8 [30.7, 37.8]	−13.8 [−15.1, −9.5]	−1.9 [−3.3, 0.7]
6	38.2 [36.5, 41.6]	−20.3 [−21.6, −18.2]	1.7 [−0.8, 4.6]
7	40.4 [36.9, 47.8]	−18.1 [−24.1, −15.1]	−7.5 [−9.6, −4.4]
8	48.7 [46.6, 53.2]	−11.5 [−13.5, −10.0]	−1.9 [−4.0, 0.5]
9	34.4 [20.0, 40.1]	−26.2 [−28.4, −20.1]	−5.9 [−7.9, −1.5]

the flexion–extension angles. In previous studies, automated methods have been developed to define joint SCSs based on joint surface geometry in the TMC joint [30], and use statistical shape modelling (SSM) to estimate lower limb geometry and pose [31]. While such methods may improve the reproducibility of SCS definition in healthy TMC joints, it is not yet clear how robust such automated methods are to changes in articular morphology, particularly in diseased TMC joints. In a *post-hoc* qualitative analysis, we found that joints with considerable joint degeneration had poorer agreement between raters compared to joints that appeared healthy. In joints that visually appeared healthy, ICC values were moderate to excellent between and within raters ($ICC > 0.5$). These results indicate that manual selection of ALs to compute TMC joint kinematics may be appropriate for healthy joints. While our results indicate only moderate reproducibility in joint angle computation using manually placed ALs, the use of automated approaches for SCS definition [30] for diseased TMC joints warrants further investigation.

In Bland–Altman analysis, we compared each rater's resulting joint angles to the mean across all raters. Applying a linear regression model to each rater's Bland–Altman plot revealed very small slopes across all raters and specimens (Table 2). While approximately half of these slopes were statistically significantly different than zero ($p < 0.05$), the small magnitude of regression slopes indicates that the difference between each rater and the average was not related to the magnitude of the average angle measurement. Further, we found that there was consistent bias between raters and the mean (Fig. 7), representative of expected differences between rater's AL placement. Whether differences detected between raters is clinically relevant warrants further investigation.

The image processing required for dynamic CT scans introduces new sources of error that are not prevalent in motion capture systems. In this study, intensity-based image registration was first performed between the HR-pQCT and dynamic CT image spaces. However, we were not able to determine an optimal set of registration parameters that visually produced adequate bone

Table 2 Slopes of regression lines plotted for Bland–Altman analysis

Specimen	Abduction–adduction Slope			Flexion–extension slope			Axial rotation slope		
	Rater 1	Rater 2	Rater 3	Rater 1	Rater 2	Rater 3	Rater 1	Rater 2	Rater 3
1	0.03	−0.01	−0.02	−0.02	0.02	0.01	−0.01	−0.02	0.01
2	0.01	0.01	−0.02	−0.01	0.02	0.01	0.00	−0.04	0.00
3	−0.03	−0.02	−0.02	0.04	0.03	0.00	−0.02	−0.01	−0.01
4	0.00	0.05	0.01	0.00	−0.05	0.04	−0.01	−0.01	−0.05
5	0.00	−0.01	0.01	0.00	0.02	−0.04	−0.01	−0.01	−0.01
6	0.02	−0.01	0.02	−0.01	0.00	−0.01	−0.01	0.01	0.00
7	−0.01	0.00	−0.02	0.01	−0.01	−0.01	0.00	0.01	0.00
8	0.02	−0.01	−0.02	−0.04	0.00	0.01	0.01	0.00	−0.02
9	0.06	−0.01	−0.03	0.00	−0.01	0.06	−0.06	0.01	−0.04

Bold indicates statistical significance, where $p < 0.05$

alignment. This was likely due to the drastic change in spatial resolution between the HR-pQCT and dynamic CT image spaces. With the addition of an intermediate registration step using static CT scans of the specimens, we were able to obtain improved bone alignment when assessed visually. Further, quantitative analysis of the TREs associated with each image registration found voxel or sub-voxel level errors, suggesting that only a small portion of the error in the joint angle results between raters was due to the image registration steps. When comparing SCS orientation between raters in the HR-pQCT and dynamic CT image space, we found little difference in the orientation of SCS axes between image spaces. This suggests that any orientation difference between SCSs defined in the HR-pQCT image space are held constant after transforming all data to the dynamic CT space, further reinforcing our confidence that the resulting difference in joint angles and translations between raters are due to rater biases when defining SCSs, not due to the image registration.

This study had several limitations. First, the dynamic CT image quality prevented the direct image segmentation and SCS definition. Our scanner was limited to a spatial resolution of $0.625 \times 0.625 \times 2.5$ mm and a longitudinal coverage of 40 mm, not enough to fully capture the MC1 bone; however, newer scanners have dynamic protocols with larger longitudinal coverage and improved spatial resolution (e.g., 160 mm longitudinal coverage, 0.625 mm³ spatial resolution). We utilized HR-pQCT scans to obtain full joint images for initial image segmentation. However, this step poses challenges in vivo due to the long scanning time and increased exposure to ionizing radiation. Instead, a high-resolution static CT scan that includes the whole bone can be obtained from other clinical CT scanners that are widely available. For example, recent developments in cone beam CT scanners allows for imaging of the hand at resolutions up to 0.2 mm³ (e.g., CurveBeam HiRise weight-bearing CT scanners), which may be sufficient for providing a more detailed initial segmentation than images obtained from dynamic CT. Despite the additional image processing steps used here to overcome the scanner limitations, the TRE results indicate there was no substantial impact on joint angles. Second, the TMC joints in the acquired specimens varied in joint condition. Some specimens had considerable degeneration (e.g., joint space narrowing, presence of osteophytes, etc.) and others appeared healthy. We found that joint angle RMSE results were as high as 5.33° and 4.25° for inter-rater and intra-rater abduction–adduction, respectively (Fig. 8). However, the degree to which error is influenced by differences between healthy and diseased joints requires further

study. Third, while we found that repeatability was higher than reproducibility (Fig. 5, 6), it is worth noting that the repeatability analysis was only performed using one rater. This rater was considered the most experienced in terms of TMC joint anatomy among the raters in this study and therefore our improved repeatability results may reflect this. Finally, the workflow we present in this study is semi-automated, with manual corrections only needed during image segmentation when joint space is narrow. However, employing more advanced methods for image segmentation (i.e., statistical shape modelling approaches [32]) may be incorporated to completely automate the post-processing of dynamic CT datasets and further reduce processing time.

Conclusions

This work has shown that our image processing pipeline to quantify joint angles and translations from dynamic CT scans of the TMC joint is fast, repeatable, but only moderately reproducible. We found poor reproducibility of joint angle computation using our pipeline in joints that appeared diseased or had severe joint degeneration. If ALs are to be placed manually on dynamic CT datasets of diseased joints, we recommend placement of ALs by a single rater. Moreover, we recommend the use of a detailed document to ensure consistency when placing ALs. Future work will be performed to determine whether the pipeline is sufficiently sensitive to differentiate between healthy and diseased TMC joint kinematics. Moreover, the clinical significance of the difference in joint angles and translations found in this work between raters warrants further investigation. Many dynamic CT studies process their datasets using closed-source software that is not widely available (e.g., Materialise Mimics). Our open-source pipeline to quantify joint angles from dynamic CT scans requires approximately 1.5 h to completely process a single movement. Finally, this pipeline can be easily implemented for different motions, joints, and scan acquisition parameters, and can therefore enhance the utilization of dynamic CT to assess joint kinematics.

Abbreviations

3D:: Three dimensional; AL:: Anatomical landmark; CT:: Computed tomography; FLE:: Fiducial localization error; FRE:: Fiducial registration error; HR-pQCT:: High resolution peripheral computed tomography; ICC:: Intraclass correlation coefficient; JCS:: Joint coordinate system; LDT:: Lateral distal tubercle; M1TJ:: First metacarpal trapezium joint; MC1:: First metacarpal; MDT:: Medial distal tubercle; RMS:: Root mean square; RMSE:: Root mean square error; SCS:: Segment coordinate system; TM1J:: Trapezium first metacarpal joint; TM2J:: Trapezium second metacarpal joint; TMC:: Trapeziometacarpal; TRE:: Target registration error; TRP:: Trapezium; TSTJ:: Trapezium, scaphoid, trapezoid junction.

Acknowledgements

The authors would like to acknowledge the staff at the Advanced Technical Skills Simulation Laboratory at the University of Calgary for assistance in preparation of specimens used in this study.

Author contributions

MTK performed study conception, design, image acquisition, data analysis and interpretation, and manuscript writing and editing. KW performed device design and manuscript editing. JJT assisted with image acquisition and manuscript editing. TB assisted in data interpretation and manuscript editing. SLM assisted in study coordination, acquisition of materials, and manuscript editing. All authors have read and approved the final manuscript.

Funding

This research was supported by funding from the Natural Science and Engineering Research Council of Canada (MTK and SLM), the Arthritis Society (Canada) (SLM), and a Canadian Institute of Health Research Postdoctoral Fellowship (JJT).

Availability of data and materials

All scripts, code, and software used in this publication are available on GitHub: <https://github.com/ManskeLab/DYNACT>. The datasets used and/or analyzed during the current study are available from the corresponding author on reasonable request.

Declarations

Ethics approval and consent to participate

Ethics approval was obtained from the Conjoint Health Research Ethics Board at the University of Calgary was obtained (REB20-0039). The University of Calgary receives a signed Body Donation Consent Form from the legal next of kin or executor of each donor that confirms the donor's wish to assign their body to the University of Calgary's Body Donation Program. The informed consent specifies that the body may be used for medical education and/or medical research purposes.

Consent for publication

Not applicable.

Competing interests

The authors declare no competing interests.

Author details

¹Biomedical Engineering Graduate Program, Schulich School of Engineering, University of Calgary, Calgary, Canada. ²McCaig Institute for Bone and Joint Health, University of Calgary, 3280 Hospital Drive, N.W., Calgary, AB T2N 4Z6, Canada. ³Department of Radiology, Cumming School of Medicine, University of Calgary, Calgary, Canada. ⁴Biomedical Engineering Undergraduate Program, University of Waterloo, Waterloo, Canada.

Received: 13 May 2022 Accepted: 31 October 2022

Published online: 08 November 2022

References

- Cooney WP, Lucca MJ, Chao EY, Linscheid RL. The kinesiology of the thumb trapeziometacarpal joint. *J Bone Joint Surg.* 1981 [cited 2019 May 8];63:1371–81. Available from: www.jbjs.org
- Ladd AL, Weiss APC, Crisco JJ, Hagert E, Wolf JM, Glickel SZ, et al. The thumb carpometacarpal joint: anatomy, hormones, and biomechanics. *Instr Course Lect.* 2013 [cited 2019 Jun 25];62:165–79. Available from: <http://www.ncbi.nlm.nih.gov/pubmed/23395023>
- Cooney WP, Chao EY. Biomechanical analysis of static forces in the thumb during hand function. *J Bone Joint Surg Am.* 1977 Jan [cited 2019 Aug 12];59(1):27–36. Available from: <http://www.ncbi.nlm.nih.gov/pubmed/833171>
- Jónsson H, Valtýsdóttir ST, Kjartansson O, Brekkan A. Hypermobility associated with osteoarthritis of the thumb base: a clinical and radiological subset of hand osteoarthritis. *Ann Rheum Dis.* 1996 [cited 2021 Nov 3];55:540–3. Available from: <https://pubmed.ncbi.nlm.nih.gov/1010234/>
- Fontana L, Neel S, Claise JM, Ughetto S, Catilina P. Osteoarthritis of the thumb carpometacarpal joint in women and occupational risk factors: a case–control study. *J Hand Surg Am.* 2007 [cited 2019 Jun 9];32(4):459–65. Available from: <https://linkinghub.elsevier.com/retrieve/pii/S0363502307001670>
- Solovieva S, Vehmas T, Riihimäki H, Luoma K, Leino-Arjas P. Hand use and patterns of joint involvement in osteoarthritis: a comparison of female dentists and teachers. *Rheumatology.* 2005;44(4):521–8.
- Rossignol M, Leclerc A, Allaert FA, Rozenberg S, Valat JP, Avouac B, et al. Primary osteoarthritis of hip, knee, and hand in relation to occupational exposure. *Occup Environ Med.* 2005;62(11):772–7.
- D'Agostino P, Dourthe B, Kerkhof F, Harry Van Lenthe G, Stockmans F, Vereecke EE. In vivo biomechanical behavior of the trapeziometacarpal joint in healthy and osteoarthritic subjects. *Clin Biomech.* 2017;49(Sep-tember):119–27. <https://doi.org/10.1016/j.clinbiomech.2017.09.006>
- Halilaj E, Moore DC, Patel TK, Laidlaw DH, Ladd AL, Weiss APC, et al. Older asymptomatic women exhibit patterns of thumb carpometacarpal joint space narrowing that precede changes associated with early osteoarthritis. *J Biomech.* 2015 Oct 15 [cited 2019 Sep 4];48(13):3634–40. Available from: <https://www.sciencedirect.com/science/article/pii/S0021929015004492>
- Goto A, Leng S, Sugamoto K, Cooney WP, Kakar S, Zhao K. In vivo pilot study evaluating the thumb carpometacarpal joint during circumduction. *Clin Orthop Relat Res.* 2014 [cited 2019 May 8];472(4):1106–13. <https://doi.org/10.1007/s11999-013-3066-8>
- Wang KK, Zhang X, Mccombe D, Ackland DC, Ek ET, Tham SK. Quantitative analysis of in-vivo thumb carpometacarpal joint kinematics using four-dimensional computed tomography. *J Hand Surg. (European Volume).* 2018 [cited 2019 Apr 9];43(10):1088–97. Available from: www.slicer.org
- Robinson S, Straatman L, Lee TY, Suh N, Lalone E. Evaluation of four-dimensional computed tomography as a technique for quantifying carpal motion. *J Biomech Eng.* 2021;143(6).
- Brinkhorst M, Foumani M, van Rosmalen J, Selles R, Hovius S, Strackee S, et al. Four-dimensional CT analysis of carpal kinematics: an explorative study on the effect of sex and hand-dominance. *J Biomech.* 2021.
- Kerkhof FD, Vereecke EE, Vanovermeire O, Vanhaecke J, Vanneste M, Stockmans F. Trapeziometacarpal stabilization through dorsoradial ligament reconstruction: An early post-surgery in vivo biomechanical analyses. *J Orthop Res.* 2018 [cited 2020 Feb 11];36(11):2851–64. <https://doi.org/10.1002/jor.24103>
- Della Croce U, Cappozzo A, Kerrigan DC. Pelvis and lower limb anatomical landmark calibration precision and its propagation to bone geometry and joint angles. *Med Biol Eng Comput.* 1999;37(2):155–61.
- Schroeder W, Martin K, Lorensen B. The visualization toolkit, 4th ed. New York; 2006.
- McCormick M, Liu X, Jomier J, Marion C, Ibanez L. ITK: enabling reproducible research and open science. *Front Neuroinform.* 2014 Feb 20 [cited 2021 Oct 31];8(13):1–11. Available from: <https://pubmed.ncbi.nlm.nih.gov/24600387/>
- Loweckamp B, Chen D, Ibáñez L, Blezek D. The Design of SimpleITK. *Front Neuroinform.* 2013 Dec 30 [cited 2021 Oct 31];7. Available from: <https://pubmed.ncbi.nlm.nih.gov/24416015/>
- Mattes D, Haynor DR, Vesselle H, Lewellyn TK, Eubank W. Nonrigid multimodality image registration. *Medical Imaging 2001: Image Processing.* 2001;4322(2001):1609–20.
- Grood ES, Suntay WJ. A joint coordinate system for the clinical description of three-dimensional motions: application to the knee. *Transactions of the ASME.* 1983 [cited 2019 Jul 29];105:136–44. Available from: <https://biomechanical.asmedigitalcollection.asme.org>
- Cheze L, Dumas R, Comtet JJ, Rumelhart C, Fayet M. A joint coordinate system proposal for the study of the trapeziometacarpal joint kinematics. *Comput Methods Biomech Biomed Eng.* 2009 [cited 2019 Jul 29];12(3):277–82. Available from: <https://www.tandfonline.com/action/journalInformation?journalCode=gcmb20>
- Wu G, van der Helm FCT, (Dirkjan) Veeeger HEJ, Makhssous M, van Roy P, Anglin C, et al. ISB recommendation on definitions of joint coordinate systems of various joints for the reporting of human joint motion—Part II: shoulder, elbow, wrist and hand. *J Biomech.* 2005 May 1 [cited 2019 May

- 8];38(2):981–92. Available from: <https://www.sciencedirect.com/science/article/pii/S002192900400301X>
23. Yushkevich P, Piven J, Hazlett H, Smith R, Ho S, Gee J, et al. User-guided 3D active contour segmentation of anatomical structures: significantly improved efficiency and reliability. *Neuroimage*. 2006 Jul 1 [cited 2021 Oct 31];31(3):1116–28. Available from: <https://pubmed.ncbi.nlm.nih.gov/16545965/>
 24. West JB, Fitzpatrick JM, Toms SA, Maurer CR, Maciunas RJ. Fiducial point placement and the accuracy of point-based, rigid body registration. *Neurosurgery*. 2001;48(4):810–7. Available from: <https://academic.oup.com/neurosurgery/article/48/4/810/3773362>
 25. R Core Team. R: A language and environment for statistical computing. Vienna, Austria: R Foundation for Statistical Computing; 2013.
 26. Corp IBM. IBM SPSS Statistics for Windows. Armonk: SPSS Inc.; 2021.
 27. Koo TK, Li MY. A guideline of selecting and reporting intraclass correlation coefficients for reliability research. *J Chiropr Med*. 2016;15(2):155–63. Available from: <http://dx.doi.org/https://doi.org/10.1016/j.jcm.2016.02.012>
 28. Goubier JN, Devun L, Mitton D, Lavaste F, Papadogeorgou E. Normal range-of-motion of trapeziometacarpal joint. *Chir Main*. 2009;28(5):297–300.
 29. Halilaj E, Moore DC, Laidlaw DH, Got CJ, Weiss APC, Ladd AL, et al. The morphology of the thumb carpometacarpal joint does not differ between men and women, but changes with aging and early osteoarthritis. *J Biomech*. 2014 Aug 22 [cited 2019 Jun 10];47(11):2709–14. Available from: <https://www.sciencedirect.com/science/article/pii/S0021929014002863>
 30. Halilaj E, Rainbow MJ, Got CJ, Moore DC, Crisco JJ. A thumb carpometacarpal joint coordinate system based on articular surface geometry. *J Biomech*. 2013 Mar 15 [cited 2019 Jul 29];46(5):1031–4. Available from: <https://www.sciencedirect.com/science/article/pii/S0021929012007270>
 31. Zhang J, Fernandez J, Hislop-Jambrich J, Besier TF. Lower limb estimation from sparse landmarks using an articulated shape model. *J Biomech*. 2016;49(16):3875–81.
 32. Schneider MTY, Zhang J, Crisco JJ, Weiss A peter C, Amy L, Nielsen PMF, et al. Automatic segmentation of the thumb trapeziometacarpal joint using parametric statistical shape modelling and random forest regression voting. *Comput Methods Biomech Biomed Eng Imaging Vis*. 2020;7(3):297–301.

Publisher's Note

Springer Nature remains neutral with regard to jurisdictional claims in published maps and institutional affiliations.

Ready to submit your research? Choose BMC and benefit from:

- fast, convenient online submission
- thorough peer review by experienced researchers in your field
- rapid publication on acceptance
- support for research data, including large and complex data types
- gold Open Access which fosters wider collaboration and increased citations
- maximum visibility for your research: over 100M website views per year

At BMC, research is always in progress.

Learn more biomedcentral.com/submissions

